Volume 2
Number 5
September 2022
Pages 765–1238

Environmental Science
Atmospheres

rsc.li/esatmospheres

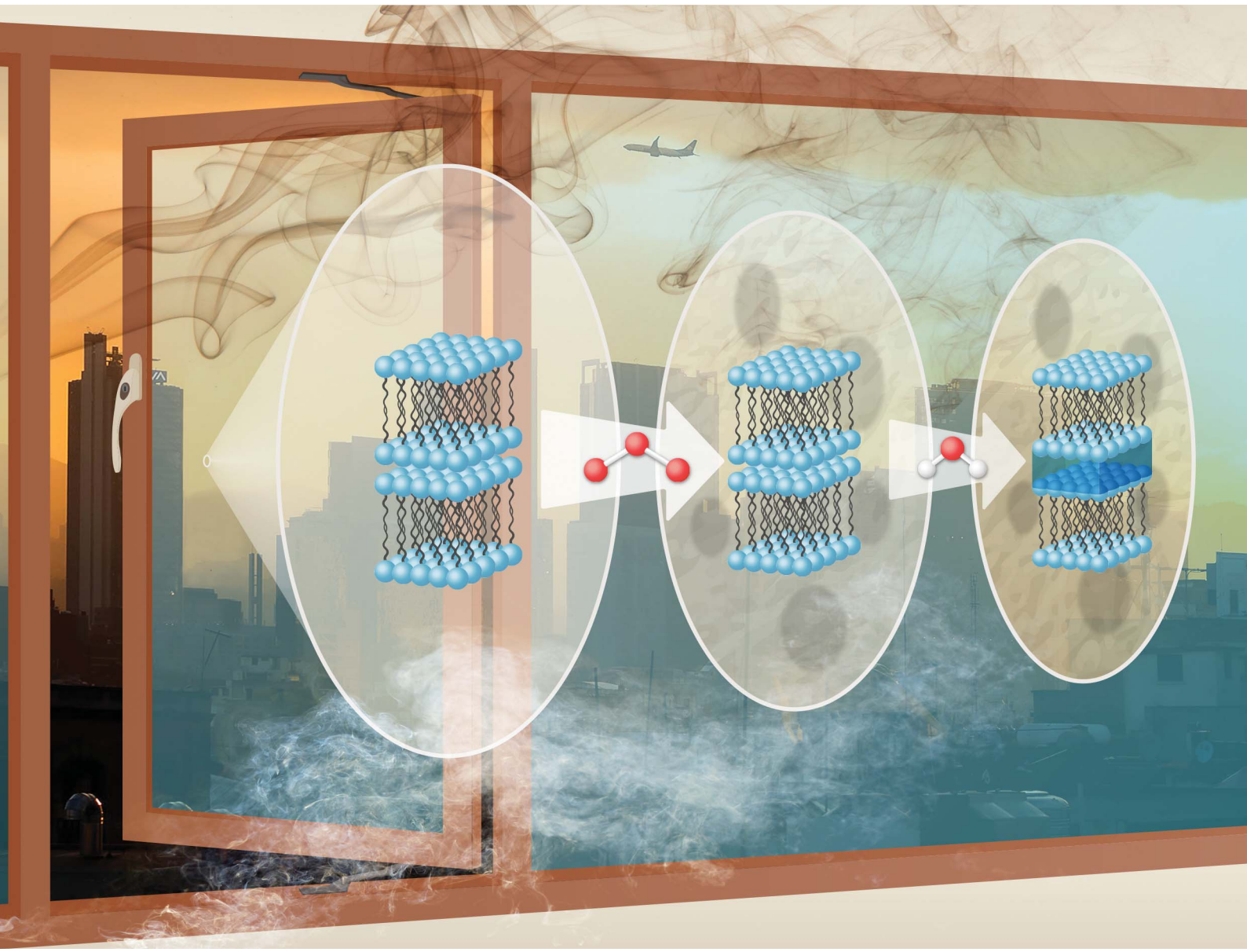

ISSN 2634-3606

ROYAL SOCIETY OF CHEMISTRY

PAPER
Christian Pfrang *et al.*
The evolution of surface structure during simulated atmospheric ageing of nano-scale coatings of an organic surfactant aerosol proxy

Environmental Science: Atmospheres

ROYAL SOCIETY OF CHEMISTRY

PAPER

View Article Online
View Journal | View Issue

Cite this: *Environ. Sci.: Atmos.*, 2022, **2**, 964

The evolution of surface structure during simulated atmospheric ageing of nano-scale coatings of an organic surfactant aerosol proxy†

Adam Milsom, [a] Adam M. Squires, [b] Maximilian W. A. Skoda, [c] Philipp Gutfreund, [d] Eleonore Mason, [be] Nicholas J. Terrill [e] and Christian Pfrang *[af]

Atmospheric aerosol particles can be coated with organic materials, impacting aerosol atmospheric lifetime and urban air quality. Coatings of organic materials are also found on indoor surfaces such as window glass. Oleic acid is a fatty acid surfactant that is abundant in cooking and marine aerosol emissions. Under ambient conditions it can self-assemble into lamellar bilayers (stacks) with its sodium salt. We found that nano-scale oleic acid–sodium oleate films spin-coated onto solid silicon substrates form a mixed-phase area of lamellar stacks and amorphous films. The coatings were subjected to simulated atmospheric ageing (ozonolysis and humidity changes) while the surface structure was followed by neutron reflectometry. We found that the orientation of lamellar stacks, which is known to affect the diffusivity of small molecules through them, was sensitive to humidity both in oxidised and pristine films. Lamellar bilayer stacks in oxidised films acquired ~11-fold more water under humid conditions (>80% relative humidity) compared to the unoxidised film, demonstrating a significant increase in film hygroscopicity after oxidation. Lamellar stacks, consisting only of starting materials, persisted at the end of simulated atmospheric ageing. These findings for atmospherically relevant nano-scale films corroborate previous work on micrometre-scale layers, thus demonstrating that fatty acid self-assembly could significantly increase the atmospheric lifetime of these molecules. The persistence of such semi-solid surfactant arrangements in the atmosphere has implications for the climate as well as urban and indoor air pollution.

Received 18th February 2022
Accepted 25th May 2022

DOI: 10.1039/d2ea00011c

rsc.li/esatmospheres

Environmental significance

Films of surfactant-containing organic materials are found on the surface of atmospheric aerosols and on indoor surfaces such as windows. The atmospheric lifetime of such materials is affected by the phase state, impacting the climate and urban air quality. We carried out simulated atmospheric processing (humidity change and oxidation) on nano-scale films of a semi-solid organic surfactant aerosol proxy. Using a neutron-based technique, we found that that the surface structure changes significantly with simulated atmospheric processing. Additionally, we found that an oxidised film took up ~11-fold more water at high humidity compared with a pristine film and that the surfactant material persisted after extensive oxidation. This has implications for the persistence of surfactant-containing organic emissions (*e.g.* from cooking) in the atmosphere.

1 Introduction

Aerosols contribute to ambient air pollution and affect processes such as cloud droplet formation, affecting air quality and climate.[1,2] Organic compounds can dominate aerosol composition in many parts of the world.[3] This varies with time, location, season and environment.[4–7] Poor air quality has been linked with an increased organic fraction on the surface of urban particulate matter[8] and cooking emissions have been estimated to contribute 10% to $PM_{2.5}$ emissions in the UK.[9] Away from the urban environment, organic compounds have been characterised in particulate matter from biogenic sources such as remote marine[10] and forested[11] environments. The

[a]*University of Birmingham, School of Geography, Earth and Environmental Sciences, Edgbaston, Birmingham, UK. E-mail: c.pfrang@bham.ac.uk*
[b]*University of Bath, Department of Chemistry, South Building, Soldier Down Ln, Claverton Down, Bath, UK*
[c]*ISIS Neutron and Muon Source, Science and Technology Facilities Council, Rutherford Appleton Laboratory, Didcot, OX11 0QX, UK*
[d]*Institut Laue–Langevin (ILL), 71 Avenue des Martyrs, Grenoble, 38000, France*
[e]*Diamond Light Source, Diamond House, Harwell Science and Innovation Campus, Didcot, OX11 0DE, UK*
[f]*Department of Meteorology, University of Reading, Whiteknights, Earley Gate, Reading, UK*

† Electronic supplementary information (ESI) available. See https://doi.org/10.1039/d2ea00011c

study of the effect of organic compounds on aerosol processes is therefore of global importance.

Organic surface coatings on particulate matter have been characterised in field measurements.[10,12] The reactivity of organic molecules with OH radicals has been shown to proceed faster as a particle surface coating compared with pure particles, linked with the higher surface area-to-volume ratio associated with such coatings.[13] The chemical lifetime of films of insoluble atmospheric organic materials at the air–water interface has been predicted to range from minutes to days with respect to the OH radical.[14] This could have an impact on the residence times of particulate matter, as organic coatings have been shown to prolong the lifetime of pollutants[15] and affect particle water uptake.[16] These observations highlight the importance of understanding how a particle surface film structure responds to atmospheric processing, which we address in this study.

Some organic emissions are surface active, such as fatty acids. The unsaturated fatty acid oleic acid is commonly found in cooking and marine aerosols[17–19] and fatty acids have been identified on the surface of particulate matter.[10,20,21] This makes it a suitable proxy compound for laboratory and model investigations into reactive organic aerosol systems.[22–30] The oleic acid–ozone heterogeneous oxidation system is well-studied and a simplified summary of the principal reaction and products is presented in Scheme 1.[28]

As a surfactant, oleic acid can decrease the surface tension of an aqueous particle, affecting the ability of the particle to take up water and form a cloud droplet.[31–33] Oleic acid molecules, being amphiphilic, can arrange into a range of lyotropic liquid crystal (LLC) phases in contact with water and in the presence of its sodium salt.[34,35] They can also form anhydrous lamellar bilayers (stacks) at laboratory relative humidity (RH) (~50% RH).[23] These molecular arrangements bring with them differences in viscosity and diffusivity, two factors which impact atmospheric aerosol ageing.[36,37]

Indoor surfaces can host organic compounds which are emitted by common indoor activities such as cooking, cleaning and ironing.[38,39] Organic films were shown to form on glass surfaces after exposure to cooking emissions and qualitatively shown to include oxidised and unoxidised fatty acids.[40] It has been suggested that films collected in a kitchen change surface morphology and/or form viscous phases during humidity changes.[41] Both hypotheses (morphology change and viscous phase formation) have implications for the uptake of atmospheric oxidants such as ozone due to the implied changes in surface area and film diffusivity. Oleic acid is likely present in such coatings because oleic acid and its reaction products have been followed in real-time during and after simulated cooking[18] and it is also used as a tracer for cooking emissions.[4] The surface coatings presented here can therefore be a proxy for the surface of atmospheric aerosols and organic coatings on indoor surfaces.

Fatty acid packing has been linked with hygroscopicity[16,42] and reactivity.[43–47] We have shown previously that the lamellar bilayer stack formed by the oleic acid–sodium oleate proxy slows down ozonolysis by *ca.* an order of magnitude, with thicker films reacting slower.[23] The orientation of such bilayer stacks is expected to affect the diffusion of small molecules through them. Diffusion perpendicular to the bilayer plane is orders of magnitude smaller than in-plane diffusion.[48] Bilayers are found in the dehydrated upper layer of the skin (*stratum corneum*) along with dead cells. In the context of indoor air quality, models of skin lipid-oxidant reactivity consider diffusion through this layer due to the marked decrease in molecular diffusivity,[49] which can be partially attributed to the lipid bilayers present.[50,51] These anisotropic arrangements can therefore have an impact on molecular diffusivity through them. The orientation of such bilayer arrangements is followed in this study.

Neutron and X-ray reflectometry (NR and XRR) have been used previously to probe proxy and real organic aerosol materials at the air–water interface.[14,27,52–59] These surface-sensitive techniques allow for the study of organic films down to the monolayer level. NR can be particularly sensitive to a sample if it

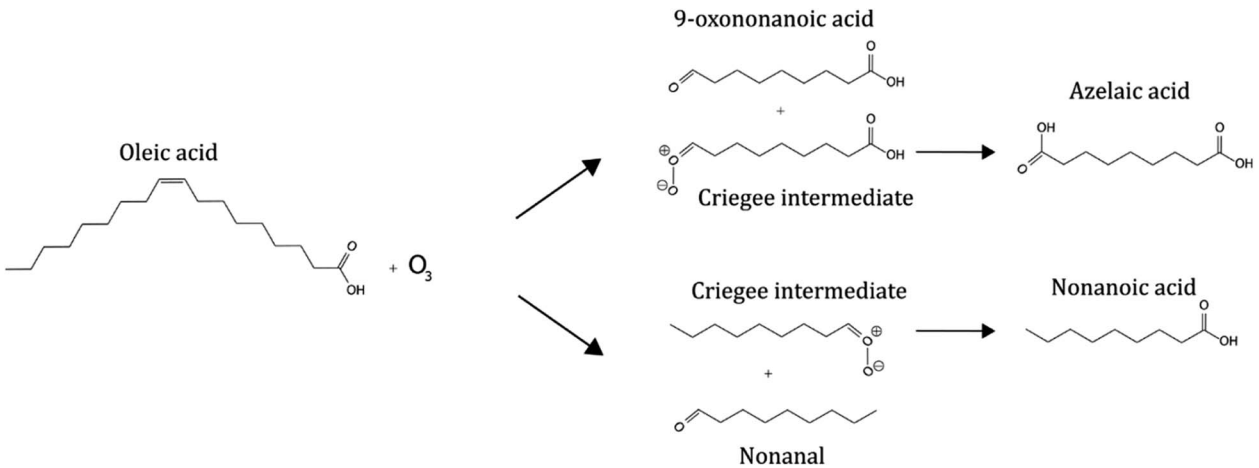

Scheme 1 The oleic acid–ozone heterogeneous reaction scheme showing the principal products.

is deuterated, due to the much larger neutron scattering power of a deuterium atom compared with a hydrogen atom.

Previous work has focussed on monolayers of deuterated oleic acid on an aqueous sub-phase,[27,55,59] self-assembly in an oleic acid–sodium oleate proxy in large levitated particles[24,60] and reaction kinetics in capillaries coated with micron-scale films of this lamellar phase proxy down to *ca.* 0.6 μm.[23] Kinetic modelling of these experiments has shown that the chemical lifetime of oleic acid could increase by days upon self-organisation.[30] Many of these studies have suggested the persistence of reacted and/or unreacted organic materials after chemical ageing – something we observe and discuss here.

In this study, we spin-coated nano-scale films of deuterated oleic acid–sodium oleate mixtures on silicon blocks with a native SiO_2 layer. This resulted in a coating with a mixed area composed of lamellar stacks and an amorphous region. We subjected these films to simulated atmospheric ageing by oxidising the sample and changing the humidity. Changes in the surface structure were followed by NR and complemented by grazing-incidence small-angle X-ray scattering (GI-SAXS) and optical microscopy. We highlight the atmospheric implications derived from these results. Our system and methodology are designed to act as a platform for the future, and more quantitative studies of the reaction kinetics and surface dynamics of such coatings.

2 Methods

Most of the techniques presented here are not commonly used in atmospherically relevant studies. The key points necessary for the understanding of each technique and what they probe are included here. More details are included in the relevant sections of the ESI.†

2.1 Preparation of spin-coated films

Deuterated oleic acid (d_{34}-OA, *Sigma-Aldrich* 98% Atom D; 99.9% purity) was used in order to provide a large contrast between the reflected neutron signal from the deposited film and the substrate required for the neutron reflectometry experiment. Sodium oleate (*Sigma-Aldrich*, 99% purity) was not deuterated. Methanol (*Sigma-Aldrich*, 99.8% purity) was used as the solvent for sample solutions. 5 cm polished silicon disks (*Crystran*, UK) were used as the substrates for these experiments. Full details of the sample preparation and spin-coating procedure are in the ESI (Section S1 ESI†). The substrate surfaces were characterised before films were deposited on them by NR and XRR, a summary of which is in the ESI (Section S2 ESI†). In total, 5 films were coated at various spin speeds (1 × 1000 rpm, 2 × 2000 rpm and 2 × 4000 rpm).

2.2 Neutron reflectometry (NR)

NR is described in detail elsewhere.[61,62] Here, we summarise the salient points of the technique. NR was carried out at the ISIS neutron and muon source (UK) on the INTER beamline and on the FIGARO beamline at the Institute Laue-Langevin (France). A schematic of the NR experiment is presented in Fig. 1(a)—note that the *x*–*z* plane is the specular plane.

NR is a technique used to probe the structure of interfaces by providing depth-resolved structural information in the form of a scattering length density (SLD) profile. Information on the thickness, roughness and density of each interfacial layer can be obtained by NR. Different isotopes have different neutron scattering lengths. The SLD of a layer is a function of the scattering length and volume fraction of each chemical component in that layer. Layered structures, *e.g.* the oleic acid–sodium oleate films on silicon studied here, give rise to steps in SLD.

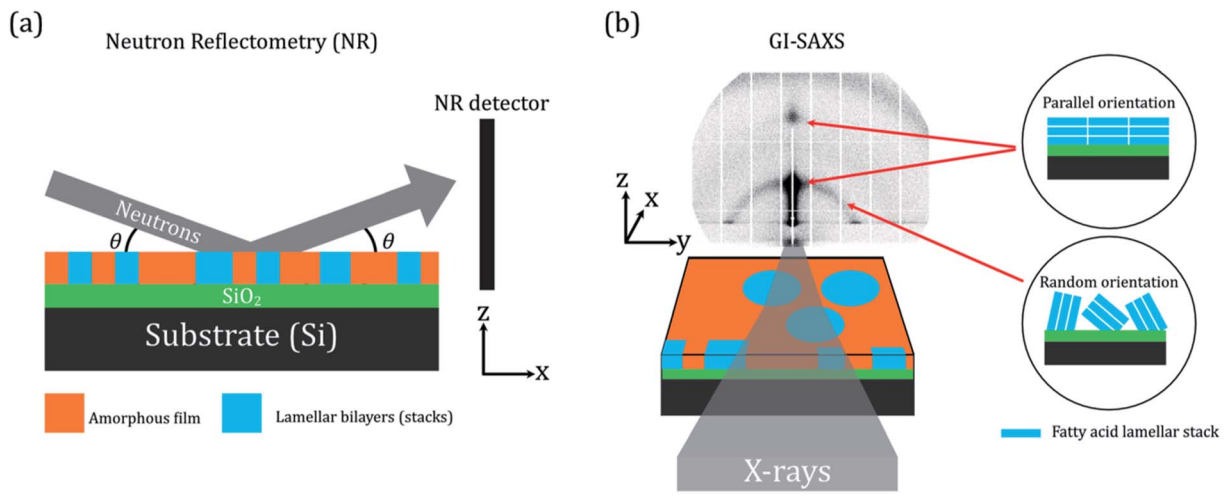

Fig. 1 Schematic representations of (a) neutron reflectometry (NR) and (b) grazing-incidence small-angle X-ray scattering (GI-SAXS) experiments. The GI-SAXS data presented are from a film coated on a silicon wafer at 2000 rpm. The mixed area model is illustrated, showing regions of the amorphous film and lamellar bilayers (stacks). The relationship between lamellar stack orientation and scattering pattern is illustrated in (b). The X-rays and neutrons travel along the *x*-axis in the positive direction, the *x*–*z* plane is the specular plane, and the angle of incidence (θ) is identified in panel (a).

The reflectivity (R – the fraction of neutrons reflected) is related to the SLD and momentum transfer (Q) *via* the formula:

$$R(Q) = \frac{16\pi^2}{Q^4}(2\ \mathrm{SLD})^2 \sin\left(\frac{Q\delta}{2}\right)^2 \quad (1)$$

This relationship is valid significantly above the critical angle, below which all neutrons are reflected. Eqn (1) is the high-Q limit for a single layer of thickness δ in air. In the case of solid-supported layers, as is the case in this study, eqn (1) is still valid if the SLD of the substrate is twice the SLD of the layer, which is roughly the case here. In general, however, the specular reflectivity has to be solved analytically using well-known optical matrix formalisms as performed here.[63] For specular reflectometry, Q is related to the neutron wavelength (λ) and angle of incidence/reflection (θ):

$$Q = \frac{4\pi}{\lambda}\sin(\theta) \quad (2)$$

Details of the NR experiments carried out in this study are presented in the ESI (Section S1, ESI†).

The chamber used to control the sample environment during NR experiments on INTER is described by Skoda *et al.*[58] In summary, the chamber: has a volume of approximately 1.5 L; has quartz windows at either end, which allow the neutrons to pass through, hit the sample and be detected on the other side; the chamber has in- and outlets, which allow the chamber to be purged with a gas—such as ozone and water vapour used in this study. The chamber used on FIGARO followed a similar design with a slightly smaller volume of 1 L and sapphire windows along the neutron path.

2.3 Grazing-incidence small-angle X-ray scattering (GI-SAXS)

GI-SAXS is closely related to NR in that small (grazing) angles of incidence are utilised to probe the surface structure of materials.[64] The GI-SAXS experiment allows for the measurement of X-ray scattering over a larger angular range and also measures off-specular scattering – this is scattering in the y-direction in Fig. 1(b). This allows us to determine the orientation of the lamellar stacks (see Fig. 1(b)). GI-SAXS was carried out on the I22 beamline at the Diamond Light Source, UK.[65] Details of the GI-SAXS experimental method are in the ESI (Section S1, ESI†).

2.4 Ozonolysis and humidity experiments

Ozone was generated by passing dry oxygen through a pre-calibrated UV pen-ray ozoniser (Ultraviolet Products Ltd, Cambridge, UK) and then to the sample chamber in which the sample was placed.

Humidity control was achieved either using a bespoke Raspberry Pi (RPi)-based system (experiments on INTER) or by varying pre-calibrated air flows of wet (D_2O) and dry N_2 flows (experiments on FIGARO). Further details of the ozonolysis and humidity control experiments are in the ESI (Section S1, ESI†).

2.5 NR model fitting

NR data are commonly analysed by fitting interfacial models to the experimental data.[61,62] Fitting rather than direct inversion is required due to the loss of phase information in the scattering process.

For all fits performed in this study, a mixed area model was selected, where the area illuminated by the neutron beam has regions of different interfacial structures (see Fig. 1 for a schematic representation). This model, consisting of a lamellar stack region and an amorphous film region, fit the best to all the films probed in this study. This was backed up by determination of the Bayesian evidence for each model,[66–69] complementary optical microscopy and GI-SAXS (see succeeding discussion and Section S1, S5 and S6, ESI†).

The *refnx* Python package[63] was used to create and fit the model to the data, optimising the model parameters with a global optimisation genetic algorithm.[70] Markov Chain Monte Carlo (MCMC) sampling of the parameter space was employed *via* the *emcee* Python package.[71] Full details of the interfacial model, model fitting procedure, MCMC and Bayesian evidence determination are provided in the ESI (Section S5, ESI†).

3 Results and discussion

3.1 The surface structure of nano-scale films

Each spin-coated film was characterised before being subjected to simulated ageing. The resulting NR curve and SLD profile for measurements taken at low and high angles (stitched together) are presented in Fig. 2 for a film coated at 4000 rpm.

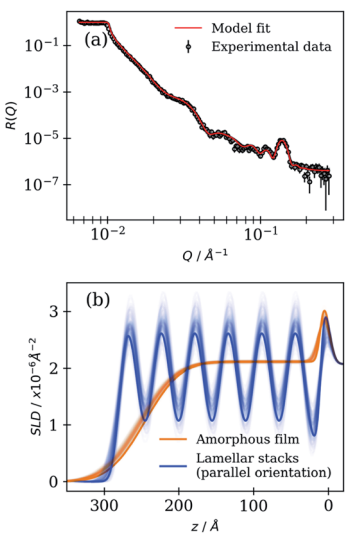

Fig. 2 (a) R *vs.* Q curve of a film coated at 4000 rpm. A model fit is presented along with 200 curves randomly sampled from the chains stored after the MCMC sampling procedure (black curves – very close to the model fit line). (b) SLD profile corresponding to the amorphous film and lamellar stack regions. SLD is plotted *vs.* the distance from the substrate surface (z). The 200 model fits from the MCMC sampling procedure are also presented to illustrate the uncertainty (fainter lines). Note that the lamellar stack region accounts for 7% of the observed signal (see Table 1).

The *R vs. Q* curve presented in Fig. 2(a) is typical of a layered interface. Fringes appear at regular intervals and the spacing between them is inversely proportional to the film thickness.[61] A Bragg peak at *ca.* 0.14 $Å^{-1}$ is observed and is consistent with the anhydrous lamellar phase Bragg peak observed in a previous SAXS study on the same non-deuterated proxy, corresponding to a lamellar bilayer thickness of *ca.* 4.5 nm.[23]

In order to quantify our confidence in our proposed model, Bayesian evidence (Z) estimation for a series of plausible model interfacial structures (including the mixed area model) was performed using the nested sampler available in the *dynesty* Python package in combination with *refnx*.[63,69] We found the greatest evidence for the mixed-area model (Fig. S5, ESI†). Details of this analysis are in the ESI (Section S5, ESI†). The mixed area model is further corroborated by the analysis of spin-coated samples prepared away from the beamline on ~3 cm^2 silicon wafers. Optical microscopy shows a mixed area with islands in the order of ~50–100 μm in diameter and complementary GI-SAXS measurements of those films exhibit lamellar stacks with both parallel (to the substrate surface) and random orientations (see Section S6, ESI†). This agrees with NR and synchrotron GI-SAXS measurements (see later).

The model reflectivity curve and SLD profile are generated using optimised parameters (Fig. 2). Additionally, curves derived from the MCMC sampling procedure that are consistent with the data illustrate the uncertainty associated with the optimised parameters and model fits. Other initial fits are presented in the ESI (Section S3, ESI†). Variations between samples in the initial amorphous film SLD are likely due to a varying ratio of deuterated oleic acid to non-deuterated sodium oleate present in the amorphous film.

The initial proportion of the sample area occupied by lamellar stacks oriented parallel to the surface was found to be between 1 and 15% for the films studied here, and the rest of the sample area being the amorphous film (Table 1). This was derived from the scale factors applied to each component of the mixed area model. Note that this does not mean that only 1 to 15% of the film is self-organised into lamellar stacks. These are fitted to specular NR curves: only reflected neutrons from repeating lamellar stacks that are parallel to the surface are detected. Model fits to experiments carried out on FIGARO returned thicker films with lower proportions of parallel lamellar stack area. The relationship between spinning speed and film thickness persists (*i.e.* lower spinning speeds result in a thicker film). However, we cannot rule out the effect of the coating environment (temperature and humidity) and substrate on the initial film structure.

Characterisation of the same system (with non-deuterated oleic acid) by GI-SAXS revealed a diffuse scattering ring in addition to the specular lamellar stack peak (see Fig. 1(b)). We are therefore confident that the lamellar stack region of the film is a mixture of both parallel and randomly oriented lamellar stacks. We discuss changes in lamellar stack orientation during simulated ageing in Section 3.2.

3.2 Simulated atmospheric ageing of nano-scale films

We simulated atmospheric ageing by exposing the spin-coated films to ozone (126–4020 ppb) and humidity (5–90% RH). Film thickness, roughness and the relative amount (scale factor) of each component can be followed using the NR model fitting procedure. All the results are summarised in Fig. 3. The NR profile of the film coated at 4000 rpm was monitored under a dry oxygen flow before oxidation to rule out potential surface structure changes only due to oxygen (Fig. 3(c), (f), (i), (l) and (o)).

3.2.1 Ozonolysis. Parallel oriented lamellar stacks persist during and after extensive oxidation (see the Bragg peak at ~0.14 $Å^{-1}$ in Fig. 3(a)–(c)). We corroborated this finding with full high and low angle NR measurements on a film after oxidation, showing a Bragg peak (Fig. S7, ESI†). The Bragg peak decreased in intensity during ozonolysis (Fig. 3(a)–(c)), which is consistent with observations made during ozonolysis of micron-scale films of the non-deuterated proxy.[23] The implications for the persistence of such surfactant organic materials are discussed in Section 4.

A slight decrease in film thickness is observed during the initial stages of ozonolysis, most evident for the film coated at 2000 rpm (Fig. 3(d)–(f)). The ozonolysis of oleic acid yields nonanal as one of the primary products. Nonanal is volatile and is assumed to be lost from the film after formation, accounting for the decrease in film thickness.[28] Generally, the drop in film thickness is small relative to the initial film thickness.

Table 1 Parameters obtained from initial model fits to NR data from spin-coated samples

Spin speed/rpm	Film thickness/nm	Film roughness/nm	No. of parallel lamellar stacks[a]	Parallel lamellar stack proportion of surface area/%
1000	51.4 ± 0.4	4.6 ± 0.1	11	15
2000[b]	43.5 ± 0.2	6.89 ± 0.04	14	7
2000	34.5 ± 0.2	2.62 ± 0.05	9	15
4000[b]	30.36 ± 0.03	4.58 ± 0.02	8	1
4000	24.4 ± 0.3	3.8 ± 0.8	6	7

[a] This is the number of repeating lamellar stacks which are oriented parallel to the substrate – only information on the parallel oriented lamellar stacks is available from these specular NR measurements. This number is also the nearest whole number of repeating stacks fitted due to the MCMC sampling returning the mean number of parallel lamellar stacks consistent with the data. [b] Data collected on the FIGARO beamline at the ILL, France.

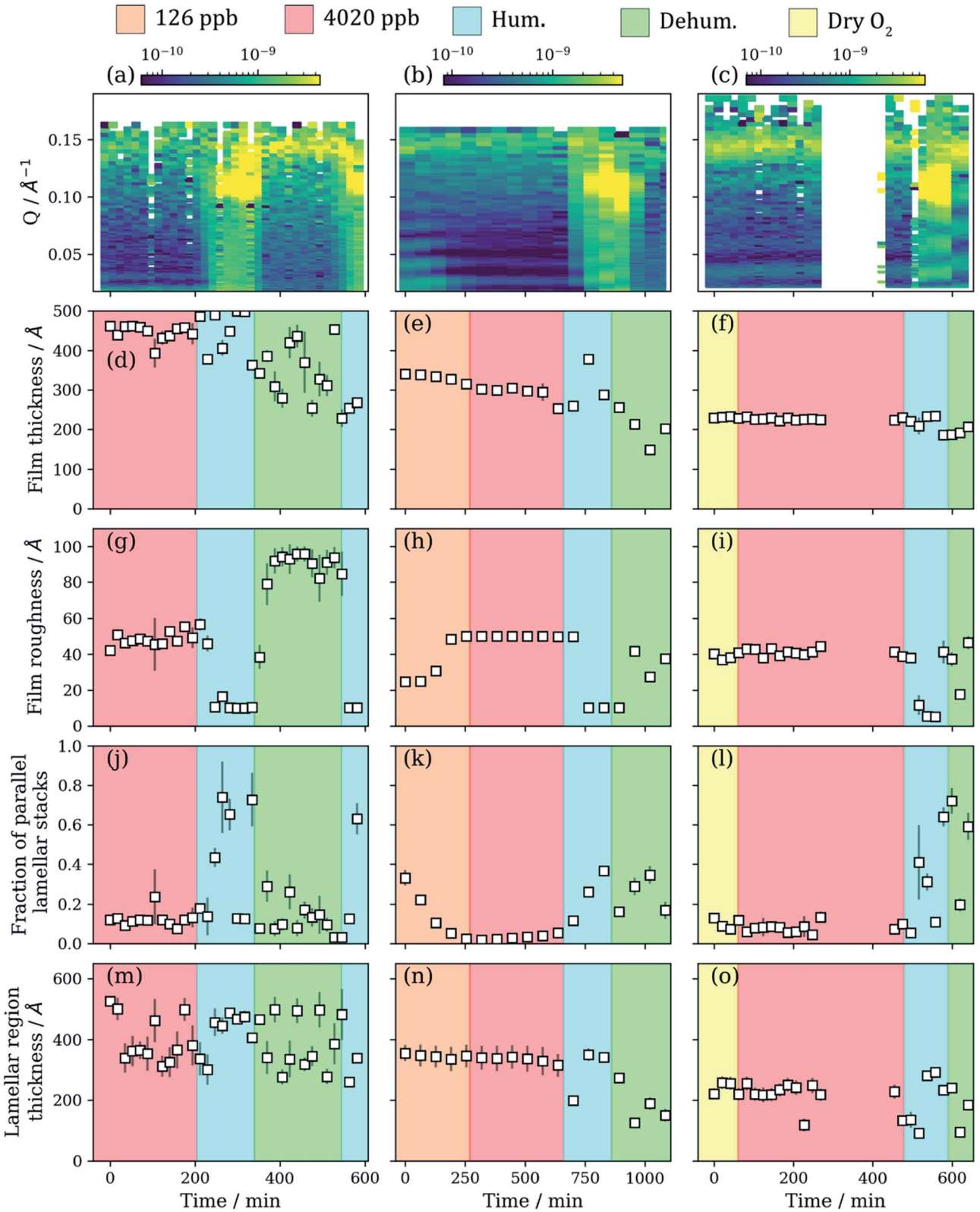

Fig. 3 Plots of RQ^4 *vs.* Q curves measured during simulated atmospheric ageing of the 3 films studied here: 1000 rpm coating (a), 2000 rpm coating (b) and 4000 rpm coating (c). Optimised parameters from model fits are plotted for each experiment: film thickness (d)–(f), film roughness (g)–(i), fraction of parallel lamellar stacks (j)–(l) and lamellar region thickness (m)–(o). The neutron beam went down for a while during film oxidation of the 4000 rpm coating (c) – parameters generally were unchanged after this period. The coloured regions correspond to ozonolysis at 126 ppb & 4020 ppb, humidification (Hum.), dehumidification (Dehum.) and dry O_2.

The change in film thickness when increasing the ozone concentration is small and negligible for the film coated at 2000 rpm (Fig. 3(e)). As ozone exposure continues, non-volatile reaction products are likely to remain in the film. Assuming the small decrease in film thickness is mostly due to the loss of nonanal from the film, the initial ozonolysis reaction is either complete or the formation of inert reaction products hinders further oleic acid ozonolysis. Note that this would be valid for the amorphous oleic acid film region and not the lamellar phase oleic acid region, which is by definition unreacted. High molecular weight products have been observed for the oleic acid–ozone reaction system.[72–75] The formation of such crusts has been postulated previously and has implications for the ageing of aerosol particles.[76,77]

A change in film thickness is observed for the lamellar phase region during ozonolysis (Fig. 3(m)–(o)). Generally, there is a decrease in lamellar region thickness as ozonolysis proceeds and this is clearest for the films coated at 1000 and 2000 rpm (Fig. 3(m) and (n)). The trend is less clear for the film coated at 4000 rpm (Fig. 3(o)). This region is modelled as stacks of lipid bilayers, and therefore any signal coming from this structure is assumed to be from the oleic acid–sodium oleate bilayer as they are the only molecules in abundance able to form a bilayer. This assumption is valid because if the 9-carbon products from the reaction form bilayers, the associated Bragg peak would appear at a much higher Q (shorter d-spacing). This has not been observed here or in SAXS experiments during ozonolysis of the same non-deuterated system.[23]

The film roughness increases with exposure to ozone (Fig. 3(g)–(i)). This is consistent for all films except for the film coated at 4000 rpm and aligns with changes in film morphology observed during the ozonolysis of pure oleic acid deposited on a substrate.[78] This implies that the surface area associated with these films also changes with time and that the surface morphology changes somewhat during ozonolysis. The atmospheric significance of this change in surface roughness is discussed in Section 4.

The relative amount of the amorphous film and oriented lamellar stacks changes during ozonolysis. The scale factors applied to each region were constrained so that their sum was the original total scale factor before ageing (±0.02) – determined by measuring the critical edge (see Fig. 2(a) maximum R region at low Q). There is an apparent decrease in the amount of oriented lamellar stacks relative to the amorphous films coated at 2000 rpm (Fig. 3(k)), though this effect is less pronounced for the thicker film coated at 1000 rpm (Fig. 3(j)). We reiterate that this scale factor is not a measure of how much of the area is covered by lamellar stacks, it only concerns the area covered by parallel oriented lamellar stacks. This is of interest due to the anisotropic diffusion characteristic of molecules through such lamellar bilayers.[48]

3.2.2 Humidification and dehumidification of oxidised and unoxidised films. More changes in the surface structure occur when humidifying and dehumidifying the oxidised films. The surface structure changed rapidly and substantially with the Bragg peak shifting to a lower Q (higher lamellar d-spacing) (Fig. 3(a)–(c)). This is due to the lamellar stacks taking up water, resulting in a thickening of the lamellar bilayers (Fig. 3(m)–(o)). Dehumidification reversed this trend and the Bragg peak moved back to its original position. This movement of the Bragg peak was reversible, suggesting that the lamellar stacks can take up water readily and reversibly (Fig. 3(a)). Regarding amorphous film thickness, the trend is not entirely reversible (Fig. 3(d)).

Reorganisation of the film and possible de-wetting from the surface is evidenced by the loss of the critical edge during humidity changes (Fig. S7 and S9, ESI†). The loss of the critical edge during humidification suggests that in-plane correlations in the surface structure occur due to surface de-wetting. This results from off-specular scattering around the critical edge, decreasing the observed specular NR signal.[79] An increase in off-specular scattering around the critical edge has been demonstrated for a polymer film de-wetting from a surface.[80] We carried out off-specular NR measurements, showing evidence of off-specular scattering occurring around the critical edge, which increased at high humidity (see Section S9, ESI†).

Reversible orientation of the lamellar stacks was observed for both oxidised and unoxidized films of the same composition. This is evident from the increase in the overall scaling factor arising from the lamellar stack region during humidification (Fig. 3(j)–(l)). Off-specular NR measurements revealed a strong specular Bragg peak signal at 82% RH for both oxidised and unoxidised films (Fig. 4(c) and (d)). This strong signal was not present at lower RH. There is also the appearance of a Bragg sheet at high RH – a diagonal streak of intensity across the specular Bragg peak (Fig. 4(c) and (d)). This is evidence of a degree of random orientation of the lamellar stacks.

Controlled humidity experiments suggest that this reversible Bragg peak shift occurs at ~80% RH (Fig. 4(c) and (d)). Measurements at RH values below this did not reveal any significant change in the size and position of the Bragg peak and Bragg sheets are not visible in the off-specular measurements at low humidity (<35% RH) for both oxidised and unoxidised films (Fig. 4(a) and (b)). This is also the case for an intermediate humidity (Fig. S8, ESI† – measurement at 63% RH). Complementary GI-SAXS measurements confirm the random orientation of lamellar stacks at room relative humidity (57% RH) (Fig. 5).

The oxidised film lamellar bilayers take up more water than the unoxidised film at high RH. The position of their respective lamellar Bragg peaks shows this (Fig. 4(e) – lower Q corresponds to a higher d-spacing, see eqn (S1)†). From the Bragg peak position, the lamellar phase d-spacing at 82% RH is 44 Å and 63 Å for the unoxidised and oxidised films, respectively. Assuming that the oleic acid–sodium oleate bilayer thickness is constant (42 ± 2 Å measured from NR model fitting of initially dry spin-coated films), the thickness of the water layer at this humidity is 2 and 21 Å for the unoxidised and oxidised films, respectively. This corresponds to bilayer stacks which take up ~11-fold more water when oxidised. Oleic acid films oxidised by ozone can be significantly more hygroscopic than unoxidised oleic acid films[81] and more oxidised compounds, measured using the O : C ratio, are known to be more hygroscopic.[82] We suggest that oxidised reaction products may have dissolved into the aqueous layer between lamellar bilayers, resulting in a more hygroscopic

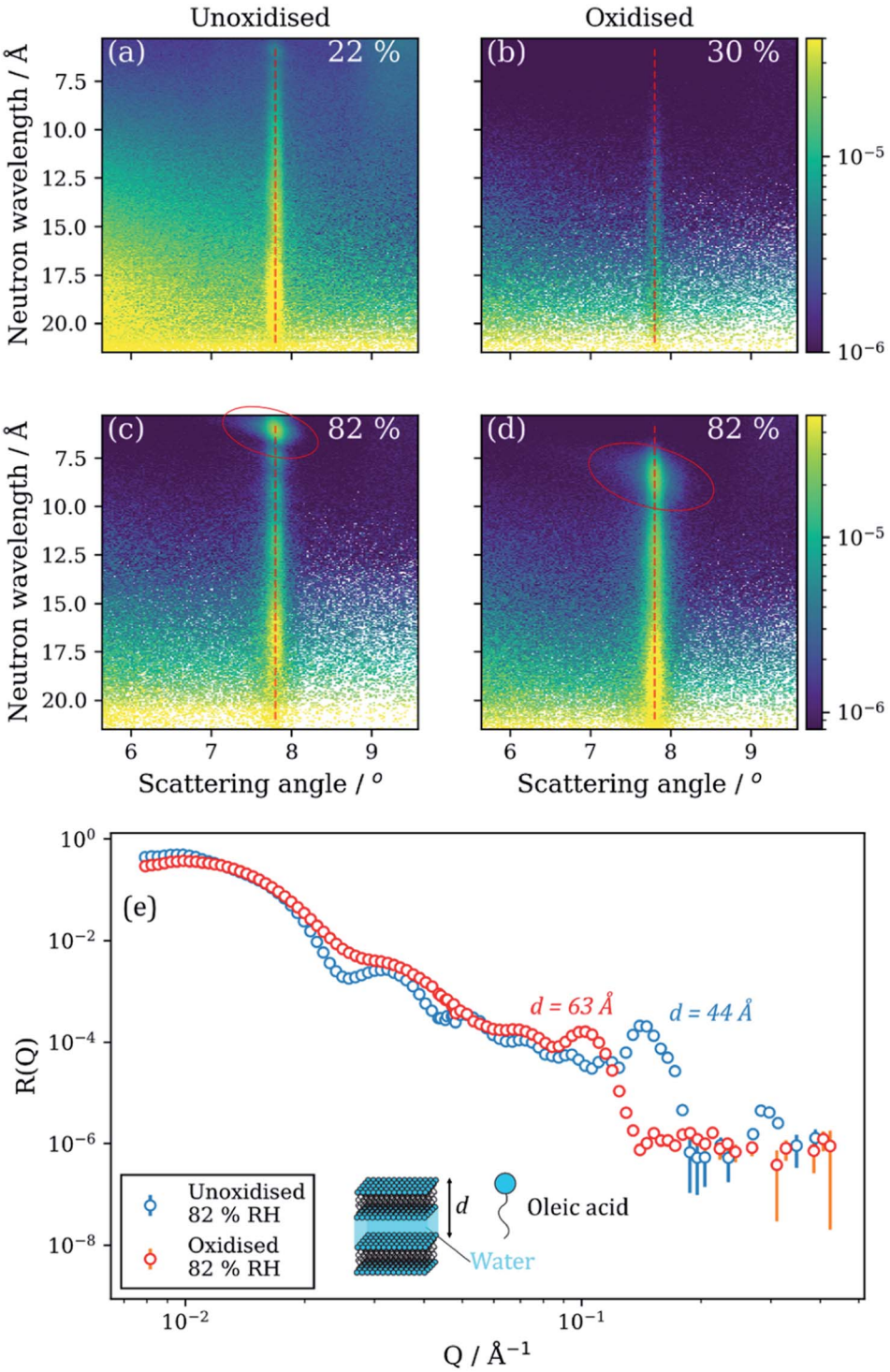

Fig. 4 Off-specular NR measurements on separate unoxidised ((a) & (c)) and oxidised ((b) & (d)) films at low and high humidity (see top right of each panel for exact RH). The specular direction is denoted by the dashed red line and the specular Bragg peak is highlighted by red circles in panels (c) and (d). (e) A comparison of 1-D specular NR curves for the oxidised and unoxidised films at 82% RH. A schematic of the lamellar bilayer is also presented along with the *d*-spacings derived from the Bragg peak position.

mixture and therefore a thicker aqueous layer. However, it was not possible to determine this directly with our NR experiments.

Complementary GI-SAXS measurements on the non-deuterated and unoxidised forms of this proxy at high RH show lamellar stack orientation and that an inverse micellar phase forms and exhibits a diffuse scattering peak at a higher Q ($\sim$0.2 Å^{-1}). Lamellar stack orientation was followed by plotting scattered intensity *vs.* the azimuthal angle in the Q-range of the

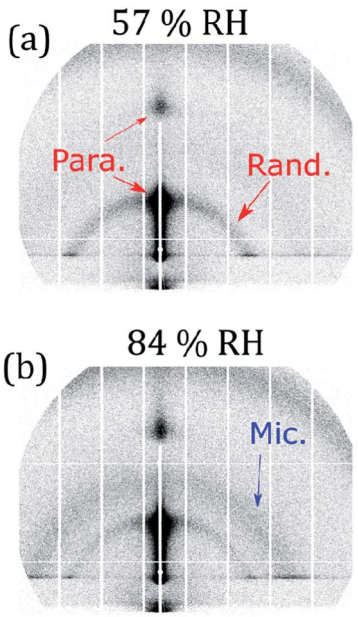

Fig. 5 2-D GI-SAXS patterns of an unoxidised film of the non-deuterated analogue of this proxy at 57% RH (a) and 84% RH (b). The scattering intensities arising from parallel (Para.) and random (Rand.) lamellar orientations are labelled accordingly in the 57% RH pattern. The inverse micellar scattering ring (Mic.) present at 84% RH is also labelled for clarity. The 2-D GI-SAXS patterns are corrected for the incident X-ray intensity and are mapped on the same intensity scale.

first order Bragg peak (see Section S9 and Fig. S9, ESI†). The ratio between specular and diffuse scattered intensity ($I_{specular}/I_{diffuse}$) is higher at high RH (an increase of ~30%). This effect is visible in the 2-D GI-SAXS patterns (Fig. 5). This higher ratio indicates an increased proportion of lamellar stacks parallel to the substrate plane, corroborating the NR results. Note that the underlying reflected X-ray beam in the specular direction also contributes to $I_{specular}$, and therefore this is a qualitative measurement.

The inverse micellar phase observed would have different physical properties compared with the lamellar stacks,[34] adding to the range of factors which change while ageing these organic coatings. Note that this inverse micellar phase peak would not be distinguishable by NR measurement due to the limited Q-range of NR experiments (see eqn (1)).

4 Atmospheric implications

Cooking emissions evolve over time and consist of both fresh and oxidised organic materials (including oleic acid).[18] Organic coatings on indoor glass surfaces can contain a mixture of oxidised and non-oxidised compounds.[40] There is a link between fatty acid packing and the key atmospheric properties of hygroscopicity[16,42] and reactivity.[43–46] In addition to the effect of lamellar phase formation on reactivity,[23] we have shown here that lamellar stacks found in both fresh and oxidised films of our proxy can orient themselves upon humidification. The diffusion of small molecules in the lamellar phase is directionally dependent, with diffusion parallel to the bilayer plane orders of magnitude higher than in the perpendicular direction.[48,83] This suggests that lamellar stacks oriented parallel to the surface present an extra hindrance to the diffusion of small molecules, such as ozone, through the organic film. This humidity-dependent change in oleic acid orientation could therefore affect the atmospheric ageing of films and particles containing oleic acid. While we did not specifically study the effect of surface hydration on the morphology of the deposited organic film, hydrated surfaces are abundant in indoor air and hydrated and non-hydrated surfaces are likely to exhibit different behaviours. A hydrated surface is more hydrophilic, and therefore the wetting behaviour of hydrophobic organic films over such surfaces could be affected by surface hydration.

The oxidation of organic coatings proceeds rapidly compared to the bulk reaction of the same species as pure particles.[13] Here, the increase in film roughness observed during oxidation implies that there is an increase in organic surface area. This larger surface area may facilitate faster uptake of reactive gases such as ozone, though information on reaction kinetics could not be extracted from these NR experiments. Deposited droplets of oleic acid have previously been observed to change morphology during ozone exposure[78] and floating monolayers of oleic acid–stearic acid can restructure during ozonolysis.[58] Such changes in organic film morphology are not widely considered in models of aerosol particle and film reaction kinetics,[25,26] though the very recent development of a kinetic multi-layer model of film formation, growth and chemistry (KM-FILM) has demonstrated a shift towards such a consideration.[84] Data from reflectometry measurements may help constrain such a model in the future.

An organic coating consisting of unreacted self-assembled oleic acid and reaction products remains deposited after simulated atmospheric ageing. This is consistent with a recent study on floating monolayers of oleic acid, where surface active products remained at the air–water interface after exposure to ozone,[27] demonstrating that this persistence of the organic film occurs both at the air–water and air–solid interfaces. The residual film is likely to be a mixture of oxidised reaction products.[28] The lamellar stack Bragg peak also remains, confirming that lamellar phase oleic acid withstands prolonged exposure to ozone[23] and that this effect is now observed in nanoscale films on a solid surface. If a surfactant material persists on particulate matter, the resulting effects on surface tension, water uptake and cloud droplet formation are also expected to persist.[31–33,85,86]

We provide direct experimental evidence that lamellar bilayers are more hygroscopic after film oxidation. The link between the oxidation state and hygroscopicity is well-established in aerosol science.[82,87] Here, we are able to estimate the effect of oxidation on the nanostructure formed by this aerosol proxy at high humidity (>80% RH). At this humidity, ~11-fold more water is present in the bilayer stacks after film oxidation compared to a "fresh" unoxidised mixture. This apparent increase in hygroscopicity suggests that water uptake and eventual cloud droplet nucleation are more likely to occur for these mixtures when oxidised.

Oleic acid ozonolysis can result in the formation of high-molecular-weight compounds.[72,74] The product film that remains after ageing may contain these oligomers, resulting in a more viscous film. An increase in viscosity has been observed experimentally for this reaction system and has been linked with the formation of such oligomers.[88] A viscous organic material in the surface layers of particulate matter has been linked to the increased long-range transport and persistence of harmful compounds found in urban particulate matter, increasing the risk to human health.[15,89] This protection is due to the reduced diffusivity of atmospheric oxidants such as ozone, limiting the extent of particle ageing. Together with our previously determined effect of self-assembly on reactivity in μm films,[23] the persistence of unreacted semi-solid materials (lamellar oleic acid) following simulated ageing in this study demonstrates that this effect is also valid for atmospherically more relevant nano-scale films.

5 Conclusions

This study has demonstrated that surface coatings of a semi-solid organic aerosol proxy undergo changes in morphology during simulated atmospheric ageing. These changes are expected to affect the uptake of trace gases into the condensed phase, especially on the nano-scale due to the increase in the surface area-to-volume ratio caused by the increasing film roughness. We highlight the importance of considering film morphology in model and experimental studies on nanoscale films.

Lamellar stacks formed by the fatty acid reversibly oriented themselves parallel to the surface with increasing humidity. This was found for both oxidised and non-oxidised films, with oxidised films taking up ~11-fold more water at high humidity compared with non-oxidised films.

The lamellar stacks persisted after simulated atmospheric ageing. This is consistent with previous findings on μm-scale films. Additionally, an amorphous film which likely consists of oxidation products also remains – consistent with recent work on floating oleic acid monolayers and confirming that film retention is also occurring at air–solid interfaces. These experiments thus demonstrate that the persistence of the semi-solid lamellar phase is valid over the micro-to-nanoscale and that oxidation products can persist down to the monolayer scale, depending on conditions.

Crucially, the NR technique does not require molecules to be assembled into 3-D nanostructures or aggregates, so that future experiments on more complex proxies and real atmospheric materials deposited on solid surfaces are possible, as long as suitable coatings can be made that are stable for the extended measurement times required for non-deuterated samples.

Data availability

The raw NR data associated with this publication can be accessed from ISIS (**https://doi.org/10.5286/ISIS.E.RB2000002**, ref. 90) and ILL (**https://doi.org/10.5291/ILL-DATA.9-10-1685**, ref. 91). Reduced data, Python scripts used for model fits and raw parameter data supporting Fig. 3 are deposited in an open-access repository (**https://doi.org/10.5281/zenodo.5748147**).

Conflicts of interest

There are no conflicts to declare.

Acknowledgements

AM acknowledges funding by NERC through the SCENARIO DTP (NE/L002566/1) and the research grant (NE/T00732X/1) for his postdoctoral fellowship; AM is also grateful for support from the NERC CENTA DTP. Jacob Boswell (University of Bath) is acknowledged for helping out at the ISIS beamtime and Ben Woden is acknowledged for helping to calibrate the ozonisers. Andrew Nelson (Australian Nuclear Science and Technology Organisation) is acknowledged for advice on the use of *refnx* for model fitting. We acknowledge the Research England funded TALENT: Technician Led Equipment Fund for enabling the offline GI-SAXS measurements. Steven Huband (University of Warwick) is acknowledged for carrying out these offline GI-SAXS measurements. Experiments at the ISIS Pulsed Neutron and Muon Source were supported by a beamtime allocation from the Science and Technology Facilities Council. This work was carried out with the support of the Diamond Light Source (DLS), instrument I22 (proposal NT23096). We are grateful to the Institut Laue-Langevin (ILL) for awarding us beamtime on the FIGARO reflectometry instrument. The computations described in this paper were performed using the University of Birmingham's BlueBEAR HPC service, which provides a High Performance Computing service to the University's research community.

References

1 U. Pöschl, Atmospheric aerosols: Composition, transformation, climate and health effects, *Angew. Chem., Int. Ed.*, 2005, **44**, 7520–7540.

2 O. Boucher, D. Randall, P. Artaxo, C. Bretherton, G. Feingold, P. Forster, V.-M. Kerminen, Y. Kondo, H. Liao, U. Lohmann, P. Rasch, S. K. Satheesh, S. Sherwood, B. Stevens and X. Y. Zhang, in *Climate Change 2013 – The Physical Science Basis*, ed. Intergovernmental Panel on Climate Change, Cambridge University Press, Cambridge, 2013, pp. 571–658.

3 J. L. Jimenez, M. R. Canagaratna, N. M. Donahue, A. S. H. Prevot, Q. Zhang, J. H. Kroll, P. F. DeCarlo, J. D. Allan, H. Coe, N. L. Ng, A. C. Aiken, K. S. Docherty, I. M. Ulbrich, A. P. Grieshop, A. L. Robinson, J. Duplissy, J. D. Smith, K. R. Wilson, V. A. Lanz, C. Hueglin, Y. L. Sun, J. Tian, A. Laaksonen, T. Raatikainen, J. Rautiainen, P. Vaattovaara, M. Ehn, M. Kulmala, J. M. Tomlinson, D. R. Collins, M. J. Cubison, J. Dunlea, J. A. Huffman, T. B. Onasch, M. R. Alfarra, P. I. Williams, K. Bower, Y. Kondo, J. Schneider, F. Drewnick, S. Borrmann, S. Weimer, K. Demerjian, D. Salcedo, L. Cottrell, R. Griffin, A. Takami, T. Miyoshi, S. Hatakeyama, A. Shimono, J. Y. Sun, Y. M. Zhang, K. Dzepina, J. R. Kimmel,

D. Sueper, J. T. Jayne, S. C. Herndon, A. M. Trimborn, L. R. Williams, E. C. Wood, A. M. Middlebrook, C. E. Kolb, U. Baltensperger and D. R. Worsnop, Evolution of Organic Aerosols in the Atmosphere, *Science*, 2009, **326**, 1525–1529.

4 Q. Wang, X. He, M. Zhou, D. D. Huang, L. Qiao, S. Zhu, Y. G. Ma, H. L. Wang, L. Li, C. Huang, X. H. H. Huang, W. Xu, D. Worsnop, A. H. Goldstein, H. Guo, J. Z. Yu, C. Huang and J. Z. Yu, Hourly Measurements of Organic Molecular Markers in Urban Shanghai, China: Primary Organic Aerosol Source Identification and Observation of Cooking Aerosol Aging, *ACS Earth Space Chem.*, 2020, **4**, 1670–1685.

5 T. Wang, R. J. Huang, Y. Li, Q. Chen, Y. Chen, L. Yang, J. Guo, H. Ni, T. Hoffmann, X. Wang and B. Mai, One-year characterization of organic aerosol markers in urban Beijing: Seasonal variation and spatiotemporal comparison, *Sci. Total Environ.*, 2020, **743**, 140689.

6 G. Li, H. Su, N. Ma, J. Tao, Y. Kuang, Q. Wang, J. Hong, Y. Zhang, U. Kuhn, S. Zhang, X. Pan, N. Lu, M. Tang, G. Zheng, Z. Wang, Y. Gao, P. Cheng, W. Xu, G. Zhou, C. Zhao, B. Yuan, M. Shao, A. Ding, Q. Zhang, P. Fu, Y. Sun, U. Pöschl and Y. Cheng, Multiphase chemistry experiment in Fogs and Aerosols in the North China Plain (McFAN): integrated analysis and intensive winter campaign 2018, *Faraday Discuss.*, 2021, **226**, 207–222.

7 P. Fu, K. Kawamura, K. Okuzawa, S. G. Aggarwal, G. Wang, Y. Kanaya and Z. Wang, Organic molecular compositions and temporal variations of summertime mountain aerosols over Mt. Tai, North China Plain, *J. Geophys. Res. Atmos.*, 2008, **113**, 1–20.

8 Y. Zhao, H. Huang, Y. Zhang, K. Wu, F. Zeng, J. Wang, X. Yu, Z. Zhu, X.-Y. Yu and F. Wang, Atmospheric particulate characterization by ToF-SIMS in an urban site in Beijing, *Atmos. Environ.*, 2020, **220**, 117090.

9 R. Ots, M. Vieno, J. D. Allan, S. Reis, E. Nemitz, D. E. Young, H. Coe, C. Di Marco, A. Detournay, I. A. Mackenzie, D. C. Green and M. R. Heal, Model simulations of cooking organic aerosol (COA) over the UK using estimates of emissions based on measurements at two sites in London, *Atmos. Chem. Phys.*, 2016, **16**, 13773–13789.

10 H. Tervahattu, Identification of an organic coating on marine aerosol particles by TOF-SIMS, *J. Geophys. Res.*, 2002, **107**, 4319.

11 J. H. Slade, A. P. Ault, A. T. Bui, J. C. Ditto, Z. Lei, A. L. Bondy, N. E. Olson, R. D. Cook, S. J. Desrochers, R. M. Harvey, M. H. Erickson, H. W. Wallace, S. L. Alvarez, J. H. Flynn, B. E. Boor, G. A. Petrucci, D. R. Gentner, R. J. Griffin and P. B. Shepson, Bouncier Particles at Night: Biogenic Secondary Organic Aerosol Chemistry and Sulfate Drive Diel Variations in the Aerosol Phase in a Mixed Forest, *Environ. Sci. Technol.*, 2019, **53**, 4977–4987.

12 E. F. Mikhailov, G. N. Mironov, C. Pöhlker, X. Chi, M. L. Krüger, M. Shiraiwa, J. D. Förster, U. Pöschl, S. S. Vlasenko, T. I. Ryshkevich, M. Weigand, A. L. D. Kilcoyne and M. O. Andreae, Chemical composition, microstructure, and hygroscopic properties of aerosol particles at the Zotino Tall Tower Observatory (ZOTTO), Siberia, during a summer campaign, *Atmos. Chem. Phys.*, 2015, **15**, 8847–8869.

13 C. Y. Lim, E. C. Browne, R. A. Sugrue and J. H. Kroll, Rapid heterogeneous oxidation of organic coatings on submicron aerosols, *Geophys. Res. Lett.*, 2017, **44**, 2949–2957.

14 R. H. Shepherd, M. D. King, A. R. Rennie, A. D. Ward, M. M. Frey, N. Brough, J. Eveson, S. Del Vento, A. Milsom, C. Pfrang, M. W. A. Skoda and R. J. L. Welbourn, Measurement of gas-phase OH radical oxidation and film thickness of organic films at the air–water interface using material extracted from urban, remote and wood smoke aerosol, *Environ. Sci. Atmos.*, 2022, DOI: **10.1039/D2EA00013J**.

15 M. Shrivastava, S. Lou, A. Zelenyuk, R. C. Easter, R. A. Corley, B. D. Thrall, P. J. Rasch, J. D. Fast, S. L. M. Simonich, H. Shen and S. Tao, Global long-range transport and lung cancer risk from polycyclic aromatic hydrocarbons shielded by coatings of organic aerosol, *Proc. Natl. Acad. Sci. U. S. A.*, 2017, **114**, 1246–1251.

16 J. Q. Xiong, M. Zhong, C. Fang, L. C. Chen and M. Lippmann, Influence of organic films on the hygroscopicity of ultrafine sulfuric acid aerosol, *Environ. Sci. Technol.*, 1998, **32**, 3536–3541.

17 A. M. P. Vicente, S. Rocha, M. Duarte, R. Moreira, T. Nunes and C. A. Alves, Fingerprinting and emission rates of particulate organic compounds from typical restaurants in Portugal, *Sci. Total Environ.*, 2021, **778**, 146090.

18 J. Zeng, Z. Yu, M. Mekic, J. Liu, S. Li, G. Loisel, W. Gao, A. Gandolfo, Z. Zhou, X. Wang, H. Herrmann, S. Gligorovski and X. Li, Evolution of Indoor Cooking Emissions Captured by Using Secondary Electrospray Ionization High-Resolution Mass Spectrometry, *Environ. Sci. Technol. Lett.*, 2020, **7**, 76–81.

19 X. Zhao, Q. Hu, X. Wang, X. Ding, Q. He, Z. Zhang, R. Shen, S. Lü, T. Liu, X. Fu and L. Chen, Composition profiles of organic aerosols from Chinese residential cooking: case study in urban Guangzhou, south China, *J. Atmos. Chem.*, 2015, **72**, 1–18.

20 R. M. Kirpes, D. Bonanno, N. W. May, M. Fraund, A. J. Barget, R. C. Moffet, A. P. Ault and K. A. Pratt, Wintertime Arctic Sea Spray Aerosol Composition Controlled by Sea Ice Lead Microbiology, *ACS Cent. Sci.*, 2019, **5**, 1760–1767.

21 H. Tervahattu, J. Juhanoja, V. Vaida, A. F. Tuck, J. V. Niemi, K. Kupiainen, M. Kulmala and H. Vehkamäki, Fatty acids on continental sulfate aerosol particles, *J. Geophys. Res. Atmos.*, 2005, **110**, 1–9.

22 P. J. Gallimore, P. T. Griffiths, F. D. Pope, J. P. Reid and M. Kalberer, Comprehensive modeling study of ozonolysis of oleic acid aerosol based on real-time, online measurements of aerosol composition, *J. Geophys. Res.*, 2017, **122**, 4364–4377.

23 A. Milsom, A. M. Squires, B. Woden, N. J. Terrill, A. D. Ward and C. Pfrang, The persistence of a proxy for cooking emissions in megacities: a kinetic study of the ozonolysis of self-assembled films by simultaneous small and wide angle X-ray scattering (SAXS/WAXS) and Raman microscopy, *Faraday Discuss.*, 2021, **226**, 364–381.

24 C. Pfrang, K. Rastogi, E. R. Cabrera-Martinez, A. M. Seddon, C. Dicko, A. Labrador, T. S. Plivelic, N. Cowieson and A. M. Squires, Complex three-dimensional self-assembly in proxies for atmospheric aerosols, *Nat. Commun.*, 2017, **8**, 1724.

25 M. Shiraiwa, C. Pfrang and U. Pöschl, Kinetic multi-layer model of aerosol surface and bulk chemistry (KM-SUB): the influence of interfacial transport and bulk diffusion on the oxidation of oleic acid by ozone, *Atmos. Chem. Phys.*, 2010, **10**, 3673–3691.

26 M. Shiraiwa, C. Pfrang, T. Koop and U. Pöschl, Kinetic multi-layer model of gas-particle interactions in aerosols and clouds (KM-GAP): linking condensation, evaporation and chemical reactions of organics, oxidants and water, *Atmos. Chem. Phys.*, 2012, **12**, 2777–2794.

27 B. Woden, M. W. A. Skoda, A. Milsom, C. Gubb, A. Maestro, J. Tellam and C. Pfrang, Ozonolysis of fatty acid monolayers at the air–water interface: organic films may persist at the surface of atmospheric aerosols, *Atmos. Chem. Phys.*, 2021, **21**, 1325–1340.

28 J. Zahardis and G. A. Petrucci, The oleic acid-ozone heterogeneous reaction system: products, kinetics, secondary chemistry, and atmospheric implications of a model system – a review, *Atmos. Chem. Phys.*, 2007, **7**, 1237–1274.

29 T. Berkemeier, A. Mishra, C. Mattei, A. J. Huisman, U. K. Krieger and U. Pöschl, Ozonolysis of Oleic Acid Aerosol Revisited: Multiphase Chemical Kinetics and Reaction Mechanisms, *ACS Earth Space Chem.*, 2021, **5**, 3313–3323.

30 A. Milsom, A. M. Squires, A. D. Ward and C. Pfrang, The impact of molecular self-organisation on the atmospheric fate of a cooking aerosol proxy, *Atmos. Chem. Phys.*, 2022, **22**, 4895–4907.

31 J. Ovadnevaite, A. Zuend, A. Laaksonen, K. J. Sanchez, G. Roberts, D. Ceburnis, S. Decesari, M. Rinaldi, N. Hodas, M. C. Facchini, J. H. Seinfeld and C. O'Dowd, Surface tension prevails over solute effect in organic-influenced cloud droplet activation, *Nature*, 2017, **546**, 637–641.

32 C. R. Ruehl and K. R. Wilson, Surface organic monolayers control the hygroscopic growth of submicrometer particles at high relative humidity, *J. Phys. Chem. A*, 2014, **118**, 3952–3966.

33 C. R. Ruehl, J. F. Davies and K. R. Wilson, Droplet Formation on Organic Aerosols, *Science*, 2016, **351**, 1447–1450.

34 G. J. T. Tiddy, Surfactant-water liquid crystal phases, *Phys. Rep.*, 1980, **57**, 1–46.

35 S. Mele, O. Söderman, H. Ljusberg-Wahrén, K. Thuresson, M. Monduzzi and T. Nylander, Phase behavior in the biologically important oleic acid/sodium oleate/water system, *Chem. Phys. Lipids*, 2018, **211**, 30–36.

36 J. P. Reid, A. K. Bertram, D. O. Topping, A. Laskin, S. T. Martin, M. D. Petters, F. D. Pope and G. Rovelli, The viscosity of atmospherically relevant organic particles, *Nat. Commun.*, 2018, **9**, 1–14.

37 M. Shiraiwa, M. Ammann, T. Koop and U. Pöschl, Gas uptake and chemical aging of semisolid organic aerosol particles-Supporting information, *Proc. Natl. Acad. Sci. U. S. A.*, 2011, **108**, 11003–11008.

38 S. Patel, S. Sankhyan, E. K. Boedicker, P. F. Decarlo, D. K. Farmer, A. H. Goldstein, E. F. Katz, W. W. Nazaroff, Y. Tian, J. Vanhanen and M. E. Vance, Indoor Particulate Matter during HOMEChem: Concentrations, Size Distributions, and Exposures, *Environ. Sci. Technol.*, 2020, **54**, 7107–7116.

39 E. D. Vicente, M. Evtyugina, A. M. Vicente, A. I. Calvo, F. Oduber, C. Blanco-Alegre, A. Castro, R. Fraile, T. Nunes, F. Lucarelli, G. Calzolai and C. A. Alves, Impact of ironing on indoor particle levels and composition, *Build. Environ.*, 2021, **192**, 107636.

40 V. W. Or, M. Wade, S. Patel, M. R. Alves, D. Kim, S. Schwab, H. Przelomski, R. O'Brien, D. Rim, R. L. Corsi, M. E. Vance, D. K. Farmer and V. H. Grassian, Glass surface evolution following gas adsorption and particle deposition from indoor cooking events as probed by microspectroscopic analysis, *Environ. Sci.: Processes Impacts*, 2020, **22**, 1698–1709.

41 H. Schwartz-Narbonne and D. J. Donaldson, Water uptake by indoor surface films, *Sci. Rep.*, 2019, **9**, 11089.

42 Q. T. Nguyen, K. H. Kjær, K. I. Kling, T. Boesen and M. Bilde, Impact of fatty acid coating on the CCN activity of sea salt particles, *Tellus Ser. B Chem. Phys. Meteorol.*, 2017, **69**, 1–15.

43 J. D. Hearn, G. D. Smith and A. J. Lovett, Ozonolysis of oleic acid particles: evidence for a surface reaction and secondary reactions involving Criegee intermediates, *Phys. Chem. Chem. Phys.*, 2005, **7**, 501–511.

44 E. P. Rosen, E. R. Garland and T. Baer, Ozonolysis of oleic acid adsorbed to polar and nonpolar aerosol particles, *J. Phys. Chem. A*, 2008, **112**, 10315–10324.

45 J. Vieceli, O. L. Ma and D. J. Tobias, Uptake and collision dynamics of gas phase ozone at unsaturated organic interfaces, *J. Phys. Chem. A*, 2004, **108**, 5806–5814.

46 E. R. Garland, E. P. Rosen, L. I. Clarke and T. Baer, Structure of submonolayer oleic acid coverages on inorganic aerosol particles: evidence of island formation, *Phys. Chem. Chem. Phys.*, 2008, **10**, 3156–3161.

47 Y. Katrib, G. Biskos, P. R. Buseck, P. Davidovits, J. T. Jayne, M. Mochida, M. E. Wise, D. R. Worsnop and S. T. Martin, Ozonolysis of mixed oleic-acid/stearic-acid particles: reaction kinetics and chemical morphology, *J. Phys. Chem. A*, 2005, **109**, 10910–10919.

48 G. Lindblom and G. Orädd, NMR Studies of translational diffusion in lyotropic liquid crystals and lipid membranes, *Prog. Nucl. Magn. Reson. Spectrosc.*, 1994, **26**, 483–515.

49 P. S. J. Lakey, A. Wisthaler, T. Berkemeier, T. Mikoviny, U. Pöschl and M. Shiraiwa, Chemical kinetics of multiphase reactions between ozone and human skin lipids: implications for indoor air quality and health effects, *Indoor Air*, 2017, **27**, 816–828.

50 T.-F. Wang, G. B. Kasting and J. M. Nitsche, A Multiphase Microscopic Diffusion Model for Stratum Corneum permeability. I Formulation, Solution, and Illustrative Results for Representative Compounds, *J. Pharm. Sci.*, 2006, **95**, 620–648.

51 T. Wang, G. B. Kasting and J. M. Nitsche, A multiphase microscopic diffusion model for stratum corneum permeability. II. Estimation of physicochemical parameters, and application to a large permeability database, *J. Pharm. Sci.*, 2007, **96**, 3024–3051.

52 C. Pfrang, F. Sebastiani, C. O. M. Lucas, M. D. King, I. D. Hoare, D. Chang and R. A. Campbell, Ozonolysis of methyl oleate monolayers at the air-water interface: oxidation kinetics, reaction products and atmospheric implications, *Phys. Chem. Chem. Phys.*, 2014, **16**, 13220–13228.

53 M. D. King, A. R. Rennie, K. C. Thompson, F. N. Fisher, C. C. Dong, R. K. Thomas, C. Pfrang and A. V. Hughes, Oxidation of oleic acid at the air-water interface and its potential effects on cloud critical supersaturations, *Phys. Chem. Chem. Phys.*, 2009, **11**, 7699–7707.

54 M. D. King, A. R. Rennie, C. Pfrang, A. V. Hughes and K. C. Thompson, Interaction of nitrogen dioxide (NO2) with a monolayer of oleic acid at the air-water interface – a simple proxy for atmospheric aerosol, *Atmos. Environ.*, 2010, **44**, 1822–1825.

55 F. Sebastiani, R. A. Campbell, K. Rastogi and C. Pfrang, Nighttime oxidation of surfactants at the air-water interface: effects of chain length, head group and saturation, *Atmos. Chem. Phys.*, 2018, **18**, 3249–3268.

56 S. H. Jones, M. D. King, A. D. Ward, A. R. Rennie, A. C. Jones and T. Arnold, Are organic films from atmospheric aerosol and sea water inert to oxidation by ozone at the air-water interface?, *Atmos. Environ.*, 2017, **161**, 274–287.

57 B. Woden, M. Skoda, M. Hagreen and C. Pfrang, Night-Time Oxidation of a Monolayer Model for the Air–Water Interface of Marine Aerosols—A Study by Simultaneous Neutron Reflectometry and in Situ Infra-Red Reflection Absorption Spectroscopy (IRRAS), *Atmosphere*, 2018, **9**, 471.

58 M. W. A. Skoda, B. Thomas, M. Hagreen, F. Sebastiani and C. Pfrang, Simultaneous neutron reflectometry and infrared reflection absorption spectroscopy (IRRAS) study of mixed monolayer reactions at the air-water interface, *RSC Adv.*, 2017, **7**, 34208–34214.

59 M. D. King, S. H. Jones, C. O. M. Lucas, K. C. Thompson, A. R. Rennie, A. D. Ward, A. A. Marks, F. N. Fisher, C. Pfrang, A. V. Hughes and R. A. Campbell, The reaction of oleic acid monolayers with gas-phase ozone at the air water interface: the effect of sub-phase viscosity, and inert secondary components, *Phys. Chem. Chem. Phys.*, 2020, **22**, 28032–28044.

60 A. Milsom, A. M. Squires, J. A. Boswell, N. J. Terrill, A. D. Ward and C. Pfrang, An organic crystalline state in ageing atmospheric aerosol proxies: Spatially resolved structural changes in levitated fatty acid particles, *Atmos. Chem. Phys.*, 2021, **21**, 15003–15021.

61 J. Penfold and R. K. Thomas, The application of the specular reflection of neutrons to the study of surfaces and interfaces, *J. Phys. Condens. Matter*, 1990, **2**, 1369–1412.

62 F. Cousin and A. Chennevière, Neutron reflectivity for soft matter, *EPJ Web Conf.*, 2018, **188**, 04001.

63 A. R. J. Nelson and S. W. Prescott, Refnx: Neutron and X-ray reflectometry analysis in python, *J. Appl. Crystallogr.*, 2019, **52**, 193–200.

64 T. Narayanan and O. Konovalov, Synchrotron Scattering Methods for Nanomaterials and Soft Matter Research, *Materials*, 2020, **13**, 752.

65 A. J. Smith, S. G. Alcock, L. S. Davidson, J. H. Emmins, J. C. Hiller Bardsley, P. Holloway, M. Malfois, A. R. Marshall, C. L. Pizzey, S. E. Rogers, O. Shebanova, T. Snow, J. P. Sutter, E. P. Williams and N. J. Terrill, I22: SAXS/WAXS beamline at Diamond Light Source - an overview of 10 years operation, *J. Synchrotron Radiat.*, 2021, **28**, 939–947.

66 A. R. McCluskey, J. F. K. Cooper, T. Arnold and T. Snow, A general approach to maximise information density in neutron reflectometry analysis, *J. Mach. Learn. Technol.*, 2020, **1**, 035002.

67 J. Skilling, Nested sampling for general Bayesian computation, *Bayesian Anal.*, 2006, **1**, 833–860.

68 J. Skilling, Nested Sampling, *AIP Conf. Proc.*, 2004, **735**, 395–405.

69 J. S. Speagle, DYNESTY: a dynamic nested sampling package for estimating Bayesian posteriors and evidences, *Mon. Not. R. Astron. Soc.*, 2020, **493**, 3132–3158.

70 P. Virtanen, R. Gommers, T. E. Oliphant, M. Haberland, T. Reddy, D. Cournapeau, E. Burovski, P. Peterson, W. Weckesser, J. Bright, S. J. van der Walt, M. Brett, J. Wilson, K. J. Millman, N. Mayorov, A. R. J. Nelson, E. Jones, R. Kern, E. Larson, C. J. Carey, İ. Polat, Y. Feng, E. W. Moore, J. VanderPlas, D. Laxalde, J. Perktold, R. Cimrman, I. Henriksen, E. A. Quintero, C. R. Harris, A. M. Archibald, A. H. Ribeiro, F. Pedregosa, P. van Mulbregt, A. Vijaykumar, A. Pietro Bardelli, A. Rothberg, A. Hilboll, A. Kloeckner, A. Scopatz, A. Lee, A. Rokem, C. N. Woods, C. Fulton, C. Masson, C. Häggström, C. Fitzgerald, D. A. Nicholson, D. R. Hagen, D. V. Pasechnik, E. Olivetti, E. Martin, E. Wieser, F. Silva, F. Lenders, F. Wilhelm, G. Young, G. A. Price, G. L. Ingold, G. E. Allen, G. R. Lee, H. Audren, I. Probst, J. P. Dietrich, J. Silterra, J. T. Webber, J. Slavič, J. Nothman, J. Buchner, J. Kulick, J. L. Schönberger, J. V. de Miranda Cardoso, J. Reimer, J. Harrington, J. L. C. Rodríguez, J. Nunez-Iglesias, J. Kuczynski, K. Tritz, M. Thoma, M. Newville, M. Kümmerer, M. Bolingbroke, M. Tartre, M. Pak, N. J. Smith, N. Nowaczyk, N. Shebanov, O. Pavlyk, P. A. Brodtkorb, P. Lee, R. T. McGibbon, R. Feldbauer, S. Lewis, S. Tygier, S. Sievert, S. Vigna, S. Peterson, S. More, T. Pudlik, T. Oshima, T. J. Pingel, T. P. Robitaille, T. Spura, T. R. Jones, T. Cera, T. Leslie, T. Zito, T. Krauss, U. Upadhyay, Y. O. Halchenko and Y. Vázquez-Baeza, SciPy 1.0: fundamental algorithms for scientific computing in Python, *Nat. Methods*, 2020, **17**, 261–272.

71 D. Foreman-Mackey, D. W. Hogg, D. Lang and J. Goodman, emcee: the MCMC Hammer, *Publ. Astron. Soc. Pac.*, 2013, **125**, 306–312.

72 J. C. Reynolds, D. J. Last, M. McGillen, A. Nijs, A. B. Horn, C. Percival, L. J. Carpenter and A. C. Lewis, Structural

analysis of oligomeric molecules formed from the reaction products of oleic acid ozonolysis, *Environ. Sci. Technol.*, 2006, **40**, 6674–6681.

73 J. Zahardis, B. W. LaFranchi and G. A. Petrucci, Photoelectron resonance capture ionization mass spectrometry of fatty acids in olive oil, *Eur. J. Lipid Sci. Technol.*, 2006, **108**, 925–935.

74 J. Zahardis, B. W. LaFranchi and G. A. Petrucci, Direct observation of polymerization in the oleic acid-ozone heterogeneous reaction system by photoelectron resonance capture ionization aerosol mass spectrometry, *Atmos. Environ.*, 2006, **40**, 1661–1670.

75 J. Zahardis, B. W. LaFranchi and G. A. Petrucci, Photoelectron resonance capture ionization-aerosol mass spectrometry of the ozonolysis products of oleic acid particles: direct measure of higher molecular weight oxygenates, *J. Geophys. Res. Atmos.*, 2005, **110**, 1–10.

76 C. Pfrang, M. Shiraiwa and U. Pöschl, Chemical ageing and transformation of diffusivity in semi-solid multi-component organic aerosol particles, *Atmos. Chem. Phys.*, 2011, **11**, 7343–7354.

77 J. W. L. Lee, V. Carrascón, P. J. Gallimore, S. J. Fuller, A. Björkegren, D. R. Spring, F. D. Pope and M. Kalberer, The effect of humidity on the ozonolysis of unsaturated compounds in aerosol particles, *Phys. Chem. Chem. Phys.*, 2012, **14**, 8023–8031.

78 H. Hung and C. Tang, Effects of Temperature and Physical State on Heterogeneous Oxidation of Oleic Acid Droplets with Ozone, *J. Phys. Chem. A*, 2010, **114**, 13104–13112.

79 R. Dalgliesh, Application of off-specular scattering of X-rays and neutrons to the study of soft matter, *Curr. Opin. Colloid Interface Sci.*, 2002, **7**, 244–248.

80 A. Castel, P. Gutfreund, B. Cabane and Y. Rharbi, Stability of fluid ultrathin polymer films in contact with solvent-loaded gels for cultural heritage, *Langmuir*, 2020, **36**, 12607–12619.

81 A. Asad, B. T. Mmereki and D. J. Donaldson, Enhanced uptake of water by oxidatively processed oleic acid, *Atmos. Chem. Phys.*, 2004, **4**, 2083–2089.

82 A. M. J. Rickards, R. E. H. Miles, J. F. Davies, F. H. Marshall and J. P. Reid, Measurements of the Sensitivity of Aerosol Hygroscopicity and the κ Parameter to the O/C Ratio, *J. Phys. Chem. A*, 2013, **117**, 14120–14131.

83 G. Lindblom and H. Wennerström, Amphiphile diffusion in model membrane systems studied by pulsed NMR, *Biophys. Chem.*, 1977, **6**, 167–171.

84 P. S. J. Lakey, C. M. A. Eichler, C. Wang, J. C. Little and M. Shiraiwa, Kinetic multi-layer model of film formation, growth, and chemistry (KM-FILM): boundary layer processes, multi-layer adsorption, bulk diffusion, and heterogeneous reactions, *Indoor Air*, 2021, **31**(6), 2070–2083.

85 M. C. Facchini, S. Decesari, M. Mircea, S. Fuzzi and G. Loglio, Surface tension of atmospheric wet aerosol and cloud/fog droplets in relation to their organic carbon content and chemical composition, *Atmos. Environ.*, 2000, **34**, 4853–4857.

86 M. C. Facchini, M. Mircea, S. Fuzzi and R. J. Charlson, Cloud albedo enhancement by surface-active organic solutes in growing droplets, *Nature*, 1999, **401**, 257–259.

87 C. Peng, Y. Wang, Z. Wu, L. Chen, R. J. Huang, W. Wang, Z. Wang, W. Hu, G. Zhang, M. Ge, M. Hu, X. Wang and M. Tang, Tropospheric aerosol hygroscopicity in China, *Atmos. Chem. Phys.*, 2020, **20**, 13877–13903.

88 N. A. Hosny, C. Fitzgerald, A. Vyšniauskas, A. Athanasiadis, T. Berkemeier, N. Uygur, U. Pöschl, M. Shiraiwa, M. Kalberer, F. D. Pope and M. K. Kuimova, Direct imaging of changes in aerosol particle viscosity upon hydration and chemical aging, *Chem. Sci.*, 2016, **7**, 1357–1367.

89 Q. Mu, M. Shiraiwa, M. Octaviani, N. Ma, A. Ding, H. Su, G. Lammel, U. Pöschl and Y. Cheng, Temperature effect on phase state and reactivity controls atmospheric multiphase chemistry and transport of PAHs, *Sci. Adv.*, 2018, **4**, eaap7314.

90 M. W. A. Skoda, A. Milsom, A. M. Squires and C. Pfrang, Self-Assembled Atmospheric Fatty Acid Aerosol Proxies: Spin-Coated Thin Film Kinetics and Phase Behaviour, *STFC ISIS Neutron and Muon Source*, 2019, DOI: **10.5286/ISIS.E.RB2000002**.

91 C. Pfrang, P. Gutfreund, A. Milsom and M. W. A. Skoda, *Hygroscopic behaviour and structural changes during ozonolysis of thin-film fatty acid aerosol proxies at realistic atmospheric conditions*, 2021, DOI: DOI: **10.5291/ILL-DATA.9-10-1685**.